Exp Fluids (2011) 50:587–595
DOI 10.1007/s00348-010-0960-7

RESEARCH ARTICLE

# Experimental study of simultaneous measurement of velocity and surface topography: in the wake of a circular cylinder at low Reynolds number

**Ivan Ng · Vaibhav Kumar · Gregory J. Sheard · Kerry Hourigan · Andreas Fouras**

Received: 29 October 2009 / Revised: 30 July 2010 / Accepted: 9 August 2010 / Published online: 22 August 2010


**Abstract** A technique to provide simultaneous measurement on both free surface topography and the velocity vector field of free surface flows is further developed and validated. Testing was performed on the topography measurement by imaging static plastic wave samples over a wide range of amplitudes. Analysis on the accuracy of the topography reconstruction, the sensitivity to noise and the dependence on spatial resolution are presented. The displacement of the free surface is insensitive to noisy input and the sensitivity shows a linear dependence with the sample spacing. Simultaneous measurements of the free surface and associated velocity field in the wake of a circular cylinder are presented for Reynolds numbers between 55 and 100.

## 1 Introduction

### 1.1 Background

Water wave visualisation is important in many industrial applications such as shipping and offshore mining. The generation and evolution of the water waves can cause vibration in and erosion of devices used in these industries. In addition, wave visualisation is highly applicable to fluvial geomorphology, which is associated with industries such as urban and agricultural constructions. Therefore, the behaviour of water waves is an important factor to be considered in the design of such components. Furthermore, the analogy between water and air in fluid dynamics is highly applicable in experimental studies of air flow in different circumstances, and it is commonly used in aerospace industries. Applications of the hydraulic analogy include an investigation of the emission of screech frequency by supersonic jet that is a potential problem for aircraft bodies (Brocher et al. 1997), and studies of screech nozzle for enhanced mixing of combustion in jet engines (Alkislar et al. 2003; Alkislar et al. 2007).

Numerous fundamental studies have been undertaken on free surface flows. These include the study of shallow flow around a circular cylinder by Fu and Rockwell (2005) and the study of supersonic jet screech by Buchanan et al. (2007), which uses the hydraulic analogy to relate the waves on a free surface to the supersonic pressure field.

According to the hydrodynamic theory for two-dimensional shallow flows, surface topography relates to the pressure field in the flow. The pressure variation, which is caused by the combination of drag force and other interactions in the fluid acceleration, results in the final topography. The simultaneous visualisation of both the pressure field and the velocity field aid the understanding of how they are related in different circumstances. It is clear that a number of fluid mechanics studies would benefit from the simultaneous measurement of both velocity field data (and related quantities such as vorticity) and the surface topography.

### 1.2 Review of free surface topography measurement

A number of methods have been developed for water wave visualisation. The simplest way to reconstruct a water

I. Ng · V. Kumar · K. Hourigan · A. Fouras (✉)
Division of Biological Engineering, Faculty of Engineering, Monash University, Clayton Campus, Melbourne, VIC 3800, Australia
e-mail: Andreas.Fouras@monash.edu

G. J. Sheard
Department of Mechanical and Aerospace Engineering, Faculty of Engineering, Monash University, Clayton Campus, Melbourne, VIC 3800, Australia

surface is to observe a number of floats in a grid. At some point in time, a photograph is taken and the depth of each float can be manually recorded. Similar approaches that detect water depth at some point include pressure, capacitance and resistance gauges (Jahne et al. 1994). These methods interfere with the flow and hence the waves, limiting the application of these methods. Non-intrusive wave visualisation on a water-table has primarily been limited to optical techniques, including stereo photography, shadowgraphy, laser slope gauges and optical displacement sensors (Brocher et al. 1997). These methods have a number of shortcomings, including poor spatial resolution, low sensitivity and yield a lack of quantitative data. Refraction techniques have been reported to have the highest sensitivity to small waves (Jahne et al. 1994). Laser slope gauges measure the gradient of a water surface by observing the refractional dislocation of a collimated laser beam between a reference (flat water) and test (wavy) condition. As the wave angle and depth increases, the laser beam is deflected or dislocated further. Appropriate inclusions of lenses into the system can remove the effect of wave depth on dislocation and yield accurate slope information (Hughes et al. 1977). Laser slope gauges are simple to create but only give 1D spatial resolution (or 2D in time) and their application is consequently limited.

This work describes the continued development of techniques to measure the surface topography of a liquid free surface. The method utilises refraction of light at the free surface as a function of the local angle of that surface. Similar methods have been developed by at least two groups. Zhang et al. (1994) have developed a system that utilises different sources of coloured light illuminating the free surface from different angles. The result is that the reflected light is colour-coded by the surface angle. Tanaka et al. (2000) developed a system that measures the distortion of a collimated speckle pattern. This in turn was based on the laser speckle techniques from which PIV itself has developed. This is a technically superior system, but does require the use of a good quality laser and a high degree of skill to create a collimated speckle pattern. The reliability and quantity of data such a system can supply is strongly coupled to the skill of the operator. De Kat et al. (2008) determined the instantaneous planar pressure fields from time-resolved velocity and acceleration fields for $Re = 9500$, behind a square-section cylinder. The technique requires integration of pressure from the momentum equation of the Navier-Stokes equations. Their study aims to provide simultaneous instantaneous velocity and topography data, and the topography is known to be highly correlated to the pressure field. PIV analysis was employed to provide simultaneous measurement of turbulent velocity field and the surface wave amplitude by Li et al. (2005). The method aimed to use tracing particles to distinguish the gas phase and the liquid phase in reconstructing surface topography, and obtaining the velocity information by a standard PIV analysis. This method is able to provide one-dimensional surface topography. Dabiri et al. (2001) and Dabiri (2003) investigated the interaction of a vertical shear layer (generated by a splitter plate with vertical surface-piercing) with the free surface and the near-surface velocity field. The free surface is measured by a free-surface gradient detector (FSGD) and the velocity field is measured by PIV. The detector colour-codes the surface slope to provide surface topography. Tsubaki et al. (2005) developed a stereoscopic method in providing two-dimensional free-surface measurement. The water is stained by white dye to obtain an opaque surface. Image pairs are captured by two cameras in stereo position to provide surface reconstruction. Cobelli et al. (2009) recently proposed a technique to provide free-surface deformation reconstructions. The technique is to image a known fringe pattern through a deformed free-surface. The reconstruction is achieved by comparing the known pattern and the deformed pattern. These two surface reconstruction techniques have capability in measuring small free-surface deformation down to $10^{-1}$ mm.

The system outlined in this paper is based on the system in Fouras et al. (2008b), itself based on the system described in Fouras et al. (2006). Fouras et al. (2006) used a frosted glass plate and Ng et al. (2010) used printed text to create a reference image. The method uses optical distortion of the frosted glass (Fouras et al. 2006) or printed text (Ng et al. 2010) imaged through the free surface to achieve the height estimation of the water surface. A similar technique was used by Moisy et al. (2009). By further combining this wave visualisation technique with the PIV measurement, Fouras et al. (2008b) advanced this technique, allowing for simultaneous measurement of velocity and surface topography. This is achieved by replacing the frosted glass with a laser sheet through the water and a camera below the water surface.

## 2 Simultaneous measurement of velocity and surface topography

### 2.1 Refraction of light and the height estimation algorithm

Light scattered by the particles are refracted by the surface gradient when passing through a wavy surface. The refracted light path causes a shift of image away from the actual particle position $\delta x$ and $\delta y$ in the x- and y-direction respectively, this is shown in Fig. 1. This inter-medium refraction obeys Snell's equation: $\eta_{air}\sin\alpha_1 = \eta_{liquid}\sin\alpha_2$, where $\eta_{air}$ and $\eta_{liquid}$ are the refractive indices of air and liquid respectively.

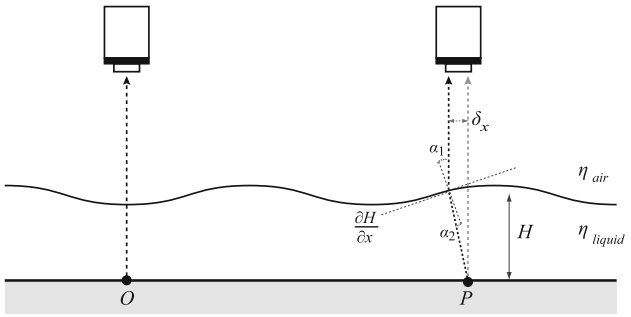


**Fig. 1** Apparent displacement vectors produced due to refraction at interface. Light ray from point $O$ passes through the inter-medium surface with zero surface gradient, the light ray is not distorted from its path and the camera captures the real position of $O$; Light ray from particle $P$ is refracted from its original path at the interface with surface gradient $\partial H/\partial x$. $\partial H/\partial x$ can then be integrated to determine the depth of the sample

To obtain local surface levels of the fluid, a height estimation algorithm was developed by modifying Snell's equation as:

$$\tan^{-1}\frac{\delta_x}{H} = \tan^{-1}\frac{\partial H}{\partial x} - \sin^{-1}\left[\eta_r \sin\left(\tan^{-1}\frac{\partial H}{\partial x}\right)\right] \quad (1)$$

where $\eta_r = \frac{\eta_{air}}{\eta_{liquid}}$.

An initial reference height $H_{\text{ref}}$ of the curved surface is given, which is the estimated mean level of the entire curved surface. Given the optical distortion measured from PIV, $\delta_x$ and $\delta_y$, at a particular point of the object, and using Eq. 1 by setting $H = H_{\text{ref}}$, one can estimate the local gradient of the curved surface $\partial H/\partial x$ and $\partial H/\partial y$. Thus, the local surface gradients can be estimated at each point on the surface. Solving this matrix of gradients with the numerical derivative estimates in $x$ and $y$ gives the estimated levels $H$ at each point. $H$ is selected in order to minimise the error between the computed distortion and the measured distortion, and the procedure is repeated until the value of $H$ converges. Applying the algorithm at each point of the surface, the entire surface profile can be determined. A full description of this algorithm can be found in Fouras et al. (2008b).

### 2.2 PIV analysis

PIV analysis is widely used in determining fluid velocity. This is achieved by tracing particles in the fluid in a series of images at different times. The trace of the particles in each pair of images is represented by a correlation function, which gives the velocity information of the fluid. A vector field is analysed from each pair of images. To obtain the surface topography of the fluid, the optical displacement must be determined as described in the previous section. This can be achieved by applying PIV analysis on the surface topography.

The key to this technique is the use of a twin-camera imaging system. The twin cameras are individually installed at the curvy surface side (top side) and the flat surface side (bottom side) of the fluid. The twins are aligned in symmetry to provide the same image field and the same magnification on the same image plane. The image plane is illuminated by a horizontal laser sheet (Sect. 5).

When the illuminated particles flow with the fluid, the bottom camera captures the non-refracted light rays scattered by the particles. Using standard PIV analysis, images from the bottom camera yield velocity fields of the fluid. Full details of the PIV algorithm used can be found in Fouras et al. (2008a).

The top camera performs simultaneous imaging with the bottom camera. These images capture the refracted light rays scattered by the particles. Refraction occurs when the light rays pass through the wavy fluid–air interface. The apparent motion of particles as viewed through the top camera combines both their true motion and effects caused by refraction. Using the same PIV analysis, the two simultaneous frames from the top and the bottom cameras are mapped to generate an optical displacement vector field. This field shows the optical distortion due to the surface gradient of the fluid. Processing the optical displacement vector field through the height estimation algorithm, the topography of the entire surface is reconstructed.

## 3 Validation with static samples

As introduced in the previous section, the advantage of this technique is that one can obtain topography information from PIV analysis. Standard PIV is normally used in the measurement of fluid dynamics. However, such flows would generate non-static surfaces. To test the performance of the technique, solid samples with known topography distribution have been used in order to provide accurate comparison between the known profile and the reconstructed profile from the PIV analyses. The solid samples are treated as an instantaneous "snapshot" in standard PIV measurement of a dynamic flow. In this section, static plastic samples with known surface profiles have been used for performing qualitative testing.

A frosted glass sheet was illuminated by a light source to disperse the light randomly, generating a random spot pattern for PIV analysis. A flat plastic sample was placed on the glass surface, the dimensions of the sample were 72.80 mm × 72.80 mm × 29.95 mm.

The frosted glass was initially captured by a CCD camera through the sample into a 2,048 pixel × 2,048 pixel image, this undistorted glass image is used as the

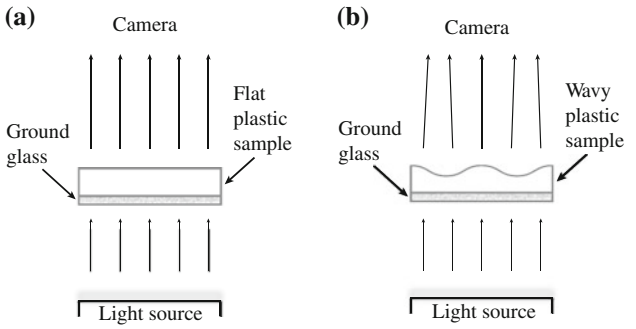


**Fig. 2** **a** The grainy pattern of the frosted glass is imaged through a flat plastic sample to obtain the undistorted reference image. **b** The distorted image of the frosted glass is imaged through the wavy plastic sample. An apparent displacement vector field is generated by correlating the two images to obtain the local level of the wavy sample surface

reference image for PIV analysis. The flat plastic was then replaced by three samples featuring wavy top surfaces of different displacements (Fig. 2).

Each image of the wavy samples was then compared with the reference image to generate the optical distortion vector field by PIV software. Using the height estimation algorithm, the distortion vector fields were integrated to give the height scalar field at each data point in the image. The free surfaces were then reconstructed from the height field using 3D plotting software. Figure 3 shows one of the samples used in the test and the result of the reconstructed wavy surface of the sample.

The three samples used in the experiment were measured by a digital height gauge, the amplitude of the waves in the samples from the digital height gauge measurement were $2.30 \pm 0.07$ mm, $1.07 \pm 0.01$ mm, $0.37 \pm 0.04$ mm. The topography results showed that the corresponding amplitudes were $2.52 \pm 0.17$ mm, $1.02 \pm 0.07$ mm and $0.38 \pm 0.03$ mm respectively, with maximum uncertainties from 6.8 to 7.7%. All three topography reconstruction results have agreement with the digital height gauge measurement results within uncertainty ranges. Figure 4 shows that the shape of the samples is faithfully reconstructed by the height estimation algorithm. The uncertainty in the topography results arise from the error of refractive index of the plastic samples. The refractive index of the plastic samples were experimentally measured by refracting a laser beam at different angles. The value measured was $1.48 \pm 0.05$ at 21°C. Note that the discrepancy is largest at the troughs of the waves. The reference height is initially assigned as the sample's depth at $x = 0$ (left side of Fig. 4), the surface amplitude along the cross-section is reconstructed relative to this depth, the greater the surface wave amplitude (i.e. troughs in these samples) results in the larger uncertainty at the corresponding data point.

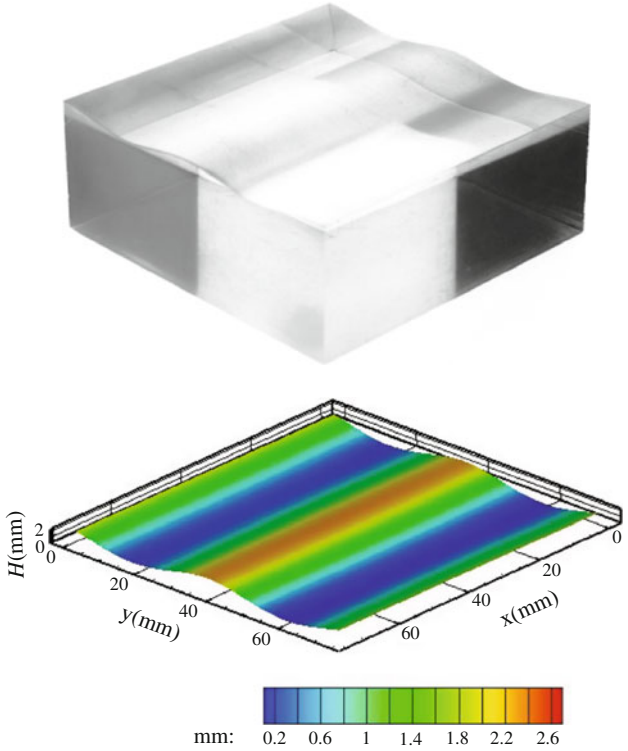


**Fig. 3** (*Top*) Photograph of the curved sample used to validate surface reconstruction. Three curved samples with different peak-trough amplitudes were tested; Surface topography of the three plastic samples tested by the height algorithm without averaging. Peak-trough distances are 2.52 mm (*bottom*), 1.02, 0.38 mm respectively. The *coloured surface* represents the level in the vertical axis, with *blue* and *red* corresponding to low and high regions respectively. The reconstruction appears to well match the actual surface

## 4 Sensitivity of the topography

Due to the importance of the optical displacement field in the height estimation algorithm, the sensitivity of the output depth to the input noise on the vector field was tested. Tests were performed by superimposing random noise onto the optical displacement vector field data, and processing the noisy data with the height estimation algorithm to obtain new depth data. These new depth data were subtracted by the original depth data and the standard deviation of the error between the two was determined. The random noise was generated from a Gaussian distribution, and tests were conducted with five levels of standard deviations of noise ranging from 0.01 to 100 pixels. Each noise input generated a noisy depth data, the result is as shown in Fig. 5. The standard deviation of the reconstructed depth, i.e. the errors in depth, has a linear dependence on the input noise. The sensitivity of this technique is defined as the ratio of the errors in depth to the errors in optical distortion, which is shown as the gradient $\partial\sigma_H/\partial\sigma_{PIV}$ of the plot in Fig. 5. The value of the gradient is constant in all three samples,

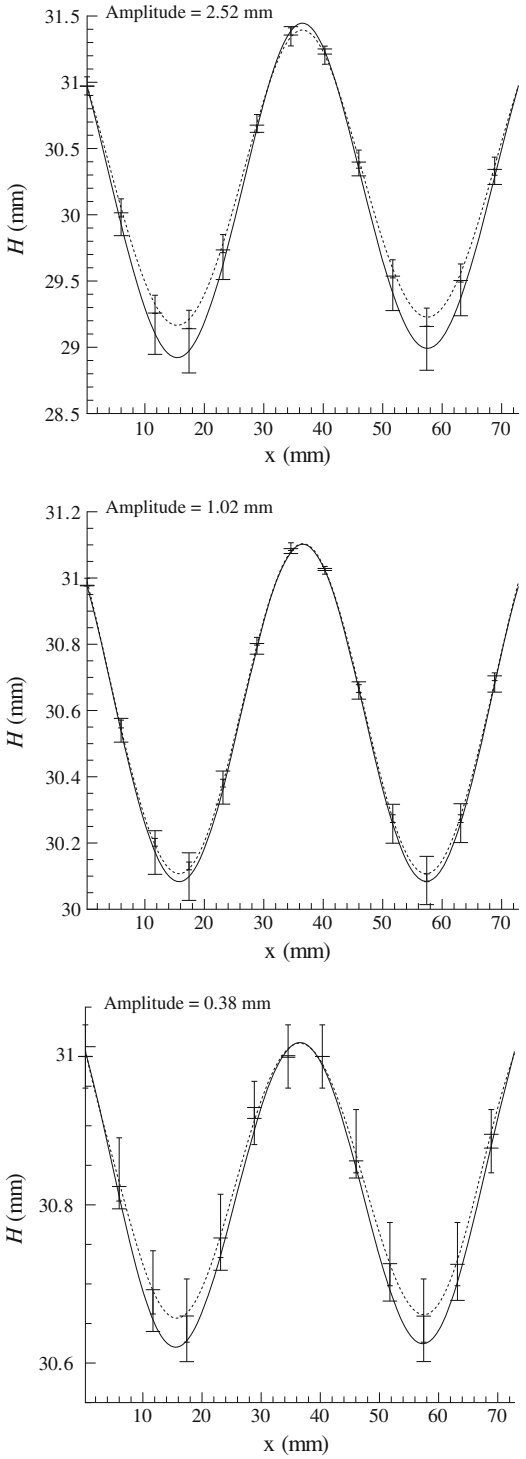


**Fig. 4** *Top* to *bottom*: Comparison between the topography reconstruction and the digital height gauge measurement of the three plastic samples, from the highest amplitude to the lowest. The curves represent the amplitude of the samples along the cross-section. *Solid line* represents the topography reconstruction, *dashed line* represents the digital gauge measurement. All three samples have agreement between the two results within the uncertainty. The height estimation algorithm reconstructed the true profile of the samples. The maximum uncertainties from the reconstructions are from 6.8 to 7.7%, these uncertainties most likely come from the error of refractive index

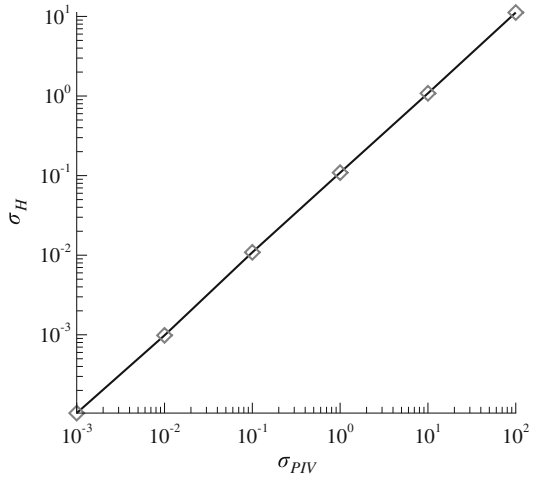


**Fig. 5** Plot of standard deviation ($\sigma$) of errors of reconstructed depth ($H$) versus standard deviation of errors of PIV vector field. The linear trend is evident over 5 decades. The gradient of the trend represents the sensitivity of the depth to the PIV optical distortion field error. The gradient of the trend is $0.112 \ll 1$, i.e. a 10% error in the optical distortion input would generate about 1% error in the reconstructed depth, this indicates that the reconstruction in depths are insensitive to the noise

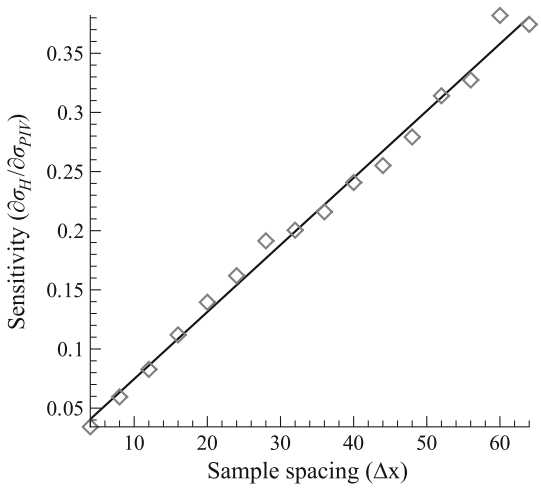


**Fig. 6** Plot of noise sensitivity versus sample spacing. Sample spacing indicates the window size (in pixels) per vector generated in PIV correlation. Increasing the window size decreases the number of vectors in the optical distortion field, hence decreasing the resolution of the topography. The sensitivity test was performed at different sample spacings showing that the noise sensitivity is linearly dependent on the sample spacing

suggesting that the sensitivity of the height estimation algorithm is independent of the sample amplitude.

In PIV analysis, the sample spacing corresponds to the resolution of the vector field generated. The sample spacing indicates the window size (pixel × pixel) to undergo particle mapping between the image pair. Each window

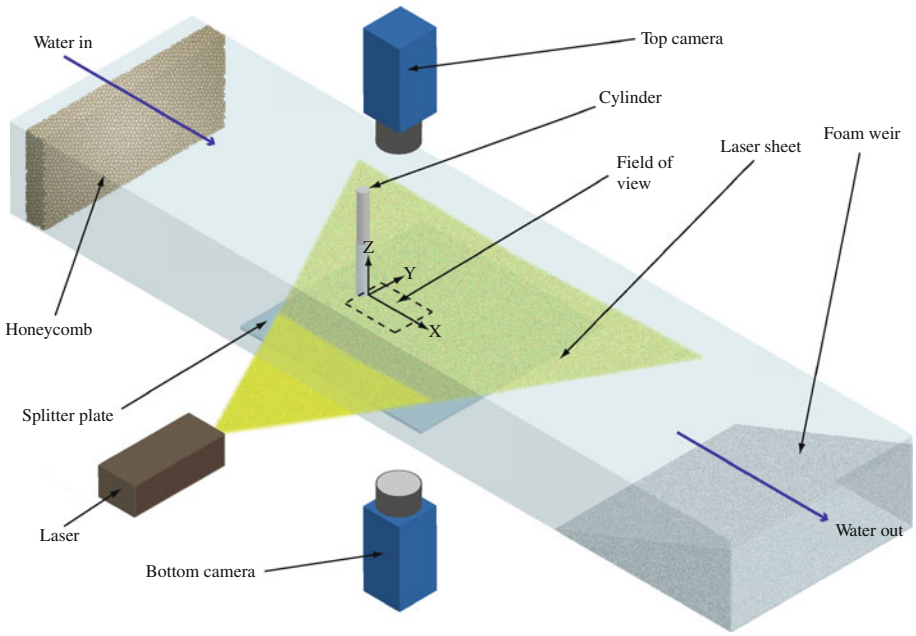


**Fig. 7** Schematic of the experiment set-up. Flow is from left to right, and the cylinder wake region is imaged by twin cameras positioned symmetrically above and below the water surface. The honeycomb is used to reduce free-stream turbulence levels. The splitter plate, 25 mm above the glass bottom, helps to reduce the size and effect of the bottom wall boundary layer on the two-dimensionality of the flow. The adjustable weir provides a means for waves to fall to the downstream reservoir, thus preventing waves from reflecting back and interfering with the normal flow. The laser sheet is 45 mm above the glass bottom

mapping generates one correlation function and hence one vector. Increasing the window size reduces the resolution of the vector field. The images of the flattest sample were processed by PIV analysis at different sample spacings. Performing the noise sensitivity test at each sample spacing level, the sensitivities were obtained, and a linear dependence with sample spacing was found, as shown in Fig. 6. The sensitivity is within the range from 0.04 to 0.37 as the sample spacing size increases from 4 to 64. This indicates that as the PIV mapping resolution reduced by a factor of 16, the reconstructed depth only became more sensitive to input noise by about a factor of 10. The reconstructed depths are therefore insensitive to the input noise on the optical distortion field.

## 5 Simultaneous measurement of height and velocity in the wake of a cylinder

A schematic of the experimental set-up is shown in Fig. 7. The water volume was seeded with particles of 25 μm in diameter. A circular cylinder of 3.9 mm in diameter was inserted on a splitter plate, positioned 25 mm above the bed of the water-table to reduce boundary layer effects. The splitter plate generates a new boundary layer by acting as a new bounding surface, which significantly reduces the ratio of the boundary layer thickness to the overall depth. This serves to increase the uniformity (two-dimensionality) of the flow at different depths. A honeycomb was located approximately 1 m upstream of the cylinder to reduce the turbulence of the incoming fluid. A foam weir was located about 2 m downstream of the cylinder to control the water level and to reduce the reflection of water waves. The depth of the water was maintained at approximately about 90 mm above the bed of the water-table throughout the experiments. The physical size of the image was 58.5 mm × 47.2 mm. The particles were illuminated by a horizontal laser sheet at a level of 45 mm above the bed of the water-table (this level is adjustable to other water depths). The wake downstream of the cylinder was recorded by a twin-camera imaging system (two pco.2000 CCD cameras). The two cameras were aligned to have the same field of view, and were mounted approximately 1 m above and below the laser sheet. The resolution of the recorded images was 1,024 × 826 pixels, with a maximum error in alignment of about 5 pixels (0.5%).

The Reynolds number of the system was obtained by the relation $Re = UD/\nu$ where $U, D$ and $\nu$ represent the upstream velocity, cylinder diameter and kinematic viscosity respectively. Experiments were performed at five different Reynolds numbers ranging between 55 and 100. Five hundred frames were recorded by the cameras at each Reynolds number, and the imaging frequency was 15.5 Hz.

At $Re = 100$, the vortex shedding behind the cylinder was highly periodic. The data were phase-averaged and are displayed in Figs. 8 and 9. The water surface deformation is magnified ($\sim 100\times$) in both figures. The axes are in the scale of cylinder diameter D, with the centre of the cylinder located at ($X/D = 0$, $Y/D = 0$). The figures clearly show the capturing of both the free-surface topography and velocity fields of this well-known flow. Figure 8 shows the free surface topography and the simultaneous velocity vector field 45 mm below the surface. The velocity vector field has a sine-wave-like pattern behind the cylinder, i.e. along $Y/D = 0$. The velocity field generates a low pressure in the wake, producing a sine-wave-like trough region on the water surface. Figure 8

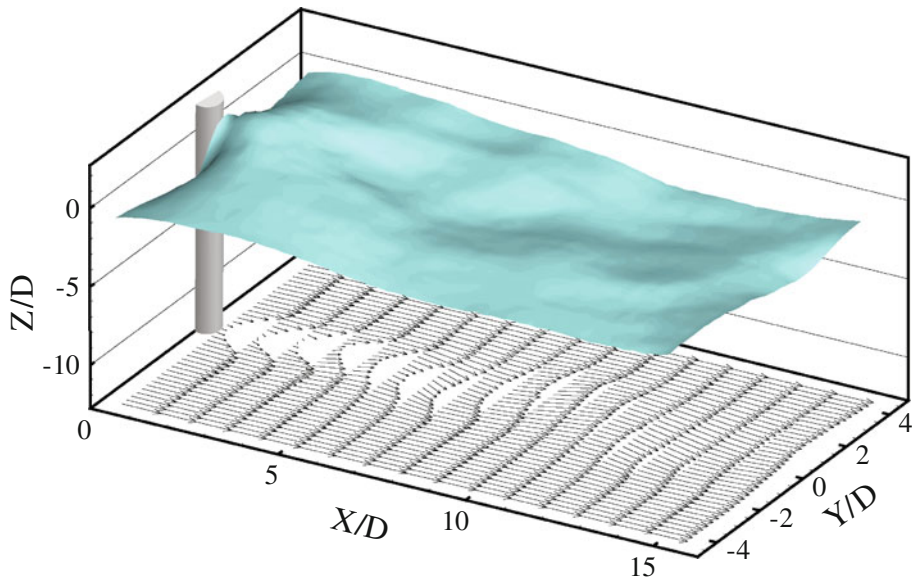


**Fig. 8** Instantaneous surface topography in the wake of a circular cylinder at Reynolds number 100, with flow from left to right and the cylinder just off the left of the image. The surface rendering is scaled in the *Z*-direction ($\sim 100\times$) to make the microscopic surface undulations observable. The vector field below shows the simultaneous velocity vector field of the water flow at a depth of 45 mm below the surface. To enhance clarity, only one in four vectors in the *X*/*D* direction are shown. Note that sine-wave-like trough region on the water surface associates with the sine-wave-like flow below

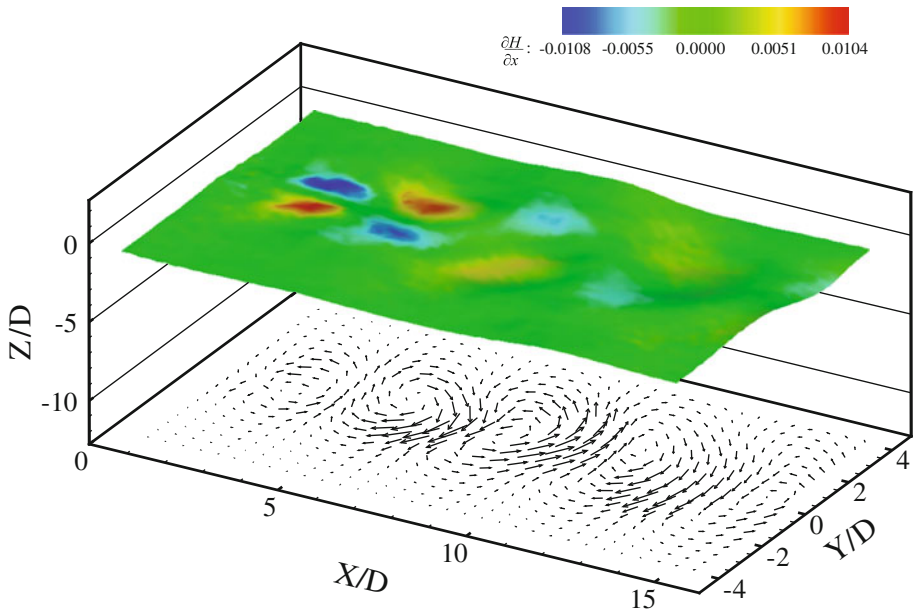


**Fig. 9** Instantaneous fluctuations of both surface topography and rebuilt velocity vector field from the time-average of data shown in Fig. 8. The contours indicate the relative surface amplitude; the colouring indicates the surface gradient in *x*-direction, gradient increases from *blue* to *red* (from negative to positive), *green* represents the zero gradient. This result indicates the relative surface amplitude and velocity vector of the time-averaged field. The peaks and troughs of the surface are symmetric and are associated with vortex propagation shown in the vector field

shows the alignment of this pattern between the submerged velocity vector field and the free surface.

Figure 9 shows fluctuations in the data presented in Fig. 8, which is obtained by subtracting the time-averaged fields from the instantaneous fields. The figure shows the vortex structure in the water flow, the surface peaks and troughs propagate along with the vortices in pairs. The vortex sheet is periodic, and similar periodic features were observed for $Re > 80$, with well-defined vortex structures behind the cylinder. Results at $Re < 57$ were only partially periodic, and the vortex structures were not observable from the data.

## 6 Adjustment of optical distortion field and limitation from the surface gradient

It is impractical to achieve a perfect alignment of the fields of view of both cameras. The misalignment between the two may be due to numerous factors, including the imperfection of the optical lenses and the surface of the water-table, the weight of the cameras distorting the bearing system and vibrations from the ground and from the camera operation altering the alignment. In general, these factors result in a positioning uncertainty of the imaging field between the cameras.

These errors are quantified by imaging a reference field of view through a flat and still water surface, and applying PIV analysis on the image pair obtained from the top and the bottom. The PIV analysis result from the flat surface should ideally have vector field of zero magnitude as no optical distortion is present. However, the experimental results indicated that a non-zero vector field of image distortion between the two cameras was generated.

The error between the two imaging fields was in the range of 0.2–0.5%, an error within 1% between the fields was readily achievable, i.e. within 10 pixels misalignment in 1,024 pixels of field dimension. As an alternative to optimising equipment to further reduce these alignment and distortion errors, a simple method is to introduce a reference field in the optical distortion analysis correcting for these measured errors.

The vectors in the reference field indicate the combined effect of systematic errors, these include the degree of misalignment between the cameras, the parallax effects in the imaging system and the imperfections on the glass surface of the water-table. 50 pairs of images were taken and were averaged into one single frame of reference for the data presented in Sect. 5. Subtracting this reference field from the measured data prior to the height estimation analysis, the surface topography result can be significantly improved. Equation 1 is derived under the assumption that the light rays in air are vertical, which is not true in the real experiment. The measured optical distortion from non-vertical rays should be affected by the parallax angle, causing an overall curvature feature across the surface measured. Such a feature is not observed in the test results of the static models presented in Figs. 3 and 4. These results show that the parallax effect has been largely negated by the reference field subtraction method. From Eq. 1, one can conclude that the topography is highly dependent on the local optical distortion $\delta x$, which contains a first order error generated in PIV analysis and a second order error caused by the misalignment. Given that the degree of misalignment was limited to a small extent, and the surface gradients of the water surface were small, this reference field subtraction method reduces the error to second order.

The amplitude of the surface gradient is the main limitation of the height estimation algorithm described in this paper. At surfaces with high amplitude of surface gradient, light rays from a particle are greatly distorted, the image position of the particle is highly shifted from its physical position, and the shape of the image is blurred and twisted. PIV analysis fails to map the particle between the top and bottom image when the optical displacement or the twisted particle size exceeds the PIV sample spacing (about 16 pixels in this paper).

Surface gradients with large amplitude can also act as a convex lens and concentrate light rays on the wavy surface. It results in a bright blurring region on the surface, blocking the cameras from imaging the particles below the surface. This phenomenon was not observed in this paper as the water surface gradient downstream of the cylinder was almost invisible, but this would be expected in experiments with high fluid velocity as the large pressure variation generally produce a large surface gradient.

## 7 Conclusions

A detailed validation of a technique to simultaneously measure both surface topography and fluid velocity has been conducted. The results show the technique to be accurate to levels of approximately 6.8–7.7% without the use of averaging, the error can be reduced by accurately measuring the refractive index of the sample. The reconstructed height is insensitive to the input noise. This noise sensitivity increases as the PIV sample spacing level increases. Additionally, the flow in the wake of a circular cylinder has been measured at five Reynolds numbers, varying from 55 to 100. These results further validate this technique and highlight the possibility of inferring the pressure field from the free-surface topography.

**Acknowledgments** The authors gratefully acknowledge the support from an Australian Research Council Discovery Grant (DP0877327).

## References

Alkislar MB, Krothapalli A, Lourenco LM (2003) Structure of a screeching rectangular jet: a stereoscopic particle image velocimetry study. J Fluid Mech 489:121–154

Alkislar MB, Krothapalli A, Butler GW (2007) The effect of streamwise vortices on the aeroacoustics of a Mach 0.9 jet. J Fluid Mech 578:139–169

Brocher E, Makhsud A (1997) New look at the screech tone mechanism of underexpanded jets. Eur J Mech B/Fluids 16: 877–891

Buchanan A, Macartney R, Thompson MC, Brocher E, Hourigan K (2007) Hydraulic analogy study of supersonic rectangular-jet screech control with cylinders. AIAA J 45(7):1539–1545

Cobelli PJ, Maurel A, Pagneux V, Petitjeans P (2009) Global measurement of water waves by Fourier transform profilometry. Exp Fluids 46(6):1037–1047

Dabiri D (2003) On the interaction of a vertical shear layer with a free surface. J Fluid Mech 480:217–232

Dabiri D, Gharib M (2001) Simultaneous free-surface deformation and near-surface velocity measurements. Exp Fluids 30(4): 381–390

de Kat R, van Oudheusden BW, Scarano F (2008) Instantaneous planar pressure field determination around a square-section cylinder based on time-resolved stereo-PIV. In: 14th international symposium on applications of laser techniques to fluid mechanics. Lisbon, Portugal

Fouras A, Hourigan K, Kawahashi M, Hirahara H (2006) An improved, free surface, topographic technique. J Vis 9(1):49–56

Fouras A, Lo Jacono D, Hourigan K (2008a) Target-free stereo PIV: a novel technique with inherent error estimation and improved accuracy. Exp Fluids 44(2):317–329. doi:10.1007/s00348-007-0404-1

Fouras A, Lo Jacono D, Sheard GJ, Hourigan K (2008b) Measurement of instantaneous velocity and surface topography in the wake of a cylinder at low Reynolds number. J Fluids Struct 24(8):1271–1277

Fu H, Rockwell D (2005) Shallow flow past a cylinder: transition phenomena at low Reynolds number. J Fluid Mech 540:75–97

Hughes BA, Grant HL, Chappell RW (1977) A fast response surface-wave slope meter and measured wind-wave moments. Deep Sea Res 24:1211–1223

Jahne B, Klinke J, Waas S (1994) Imaging of short ocean wind waves: a critical theoretical review. J Opt Soc Am A 11:2197–2209

Li FC, Kawaguchi Y, Segawa T, Suga K (2005) Simultaneous measurement of turbulent velocity field and surface wave amplitude in the initial stage of an open-channel flow by PIV. Exp Fluids 39(6):945–953

Moisy F, Rabaud M, Salsac K (2009) A synthetic Schlieren method for the measurement of the topography of a liquid interface. Exp Fluids 46(6):1021–1036

Ng I, Kumar V, Sheard GJ, Hourigan K, Fouras (2010) A surface topography of jet shock cells in a hydraulic analogy. J Vis 13(3):175–176. doi:10.1007/s12650-010-0032-3

Tanaka G, Okamoto K, Madarame H (2000) Experimental investigation on the interaction between a polymer solution jet and a free surface. Exp Fluids 29(2):178–183

Tsubaki R, Fujita I (2005) Stereoscopic measurement of a fluctuating free surface with discontinuities. Meas Sci Technol 16: 1894–1902

Zhang X, Dabiri D, Gharib M (1994) A novel technique for free surface elevation mapping. Phys Fluids 6(9):S11